Supporting Information for 'In situ synchrotron XRD investigation of the dehydration and high temperature carbonation of Ca(OH)$_2$', V. Materić, B. Ingham and R. Holt
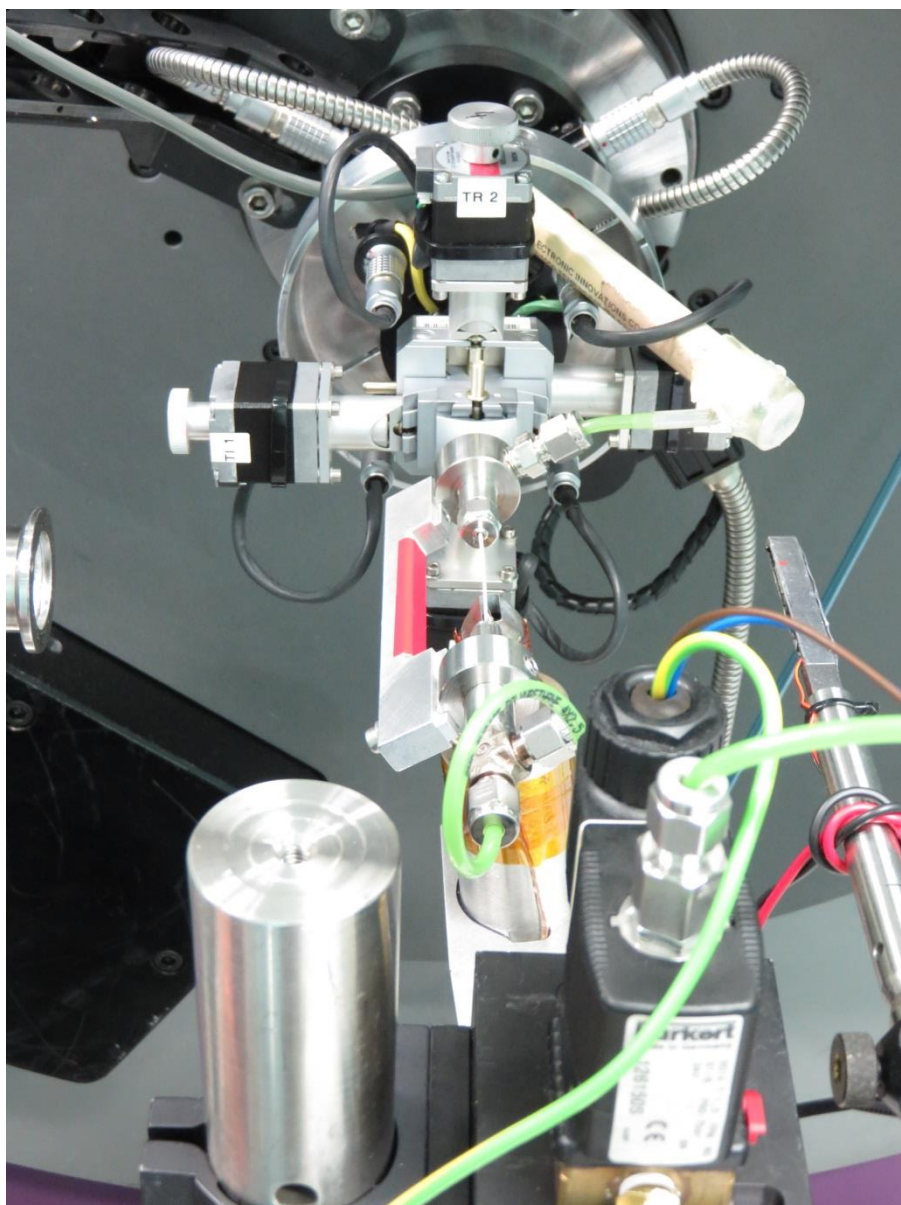
Index

1. Experiment setup

Figure S1. Photograph of the gas flow-through capillary cell used for the *in situ* XRD experiments.

2. Data processing

The Mythen detector is assembled in modules, with gaps of around 0.2° in 2θ between the modules. A full dataset can be obtained by filling the module gaps in one scan with data from a subsequent scan collected with the detector moved by 0.5°.

However, due to the rapidly changing peak intensities from one scan to the next, a slightly more sophisticated averaging method was used. Two scans collected at the same position were averaged and then combined with one at the second position collected at the intermediate time. The combination was performed by averaging all data points within a user-defined step size (0.005° increments) and dividing by the integrated incident beam signal from the I_0 ion chamber.
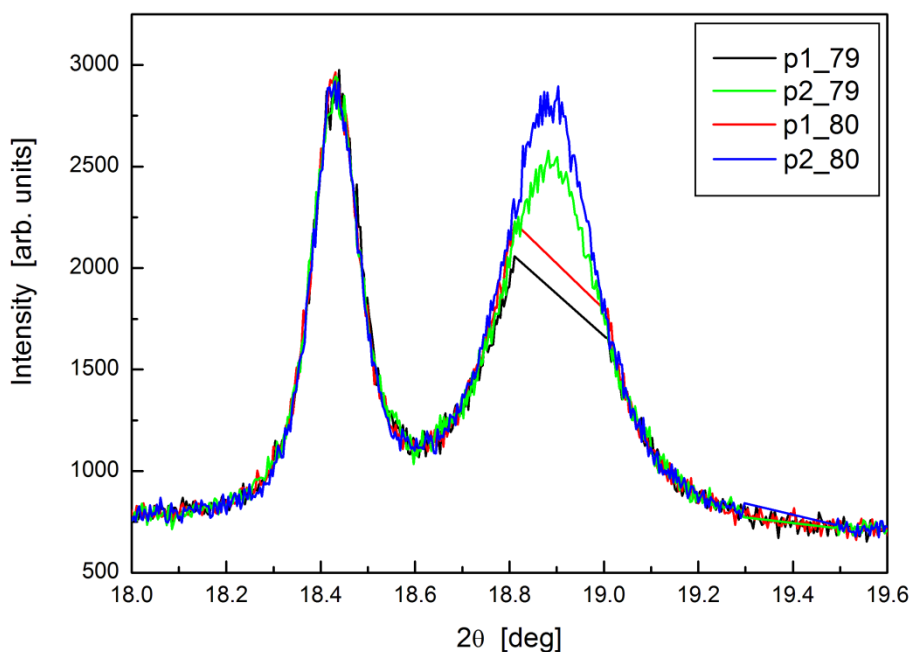
Figure S1. Raw data from $Ca(OH)_2$ heated in the presence of CO_2, showing gaps in the vicinity of the $Ca(OH)_2$ (10.0) peak at 18.4° and the growing $CaCO_3$ (10.4) peak at 18.9°. The standard method of merging would combine the black and green curves together, and the red and blue curves together. In severe cases the $CaCO_3$ peak in the merged data would have a step on either side of the gap in the raw data.

3. Data analysis

a. Peak shape

Each phase ($Ca(OH)_2$, CaO, $CaCO_3$) can be modelled independently. In all cases, the angular resolution and angular range of the data acquired using the synchrotron source was sufficient to resolve the peaks as having a Voigt shape with both Gaussian and Lorentzian size and strain components, rather than the commonly used but often over-simplified method where it is assumed that the crystallite size component is solely Lorentzian and the strain component is solely Gaussian [S1]. According to conventional Williamson-Hall analyses, crystallite size broadening has a $\cos\theta$ dependence, while strain broadening has a $\tan\theta$ dependence. Lorentzian terms are summed in a linear fashion, while Gaussian terms are summed as squares.

b. Peak width anisotropy

Plots of peak width versus the diffraction angle 2θ can be used to distinguish size and strain effects, and can also indicate the presence of any anisotropy. Examples for each of the three phases are shown in Figures S3-S5. CaO can be fitted using a simple, isotropic model. However, $Ca(OH)_2$ and $CaCO_3$ display hkl-dependent anisotropy. Various models were explored in fitting these phases.
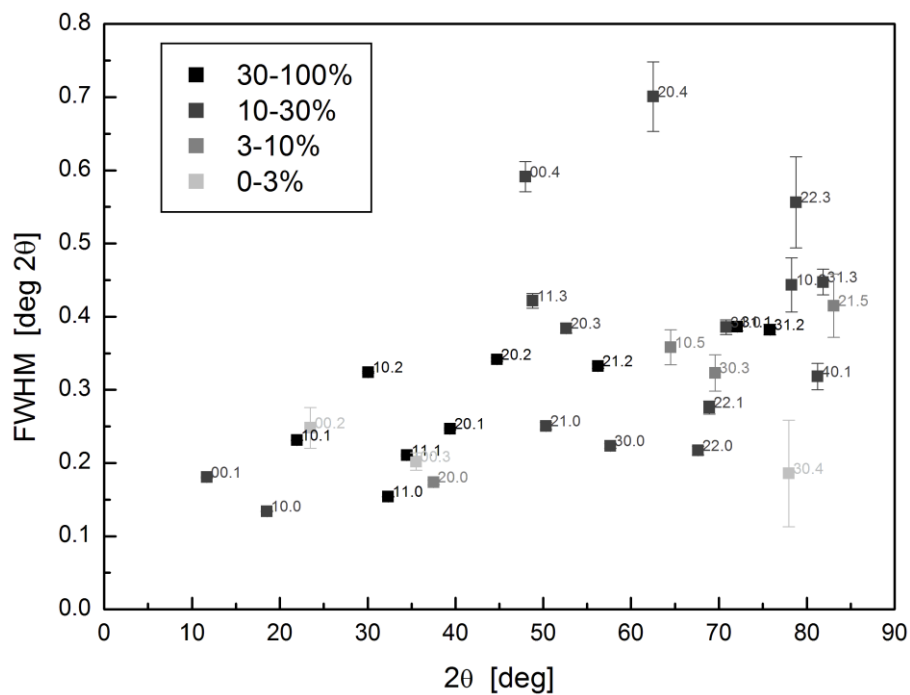
Figure S3. FWHM vs. 2θ plot for Ca(OH)$_2$ at the start of a run. The squares are coloured in grayscale to reflect their relative intensity.
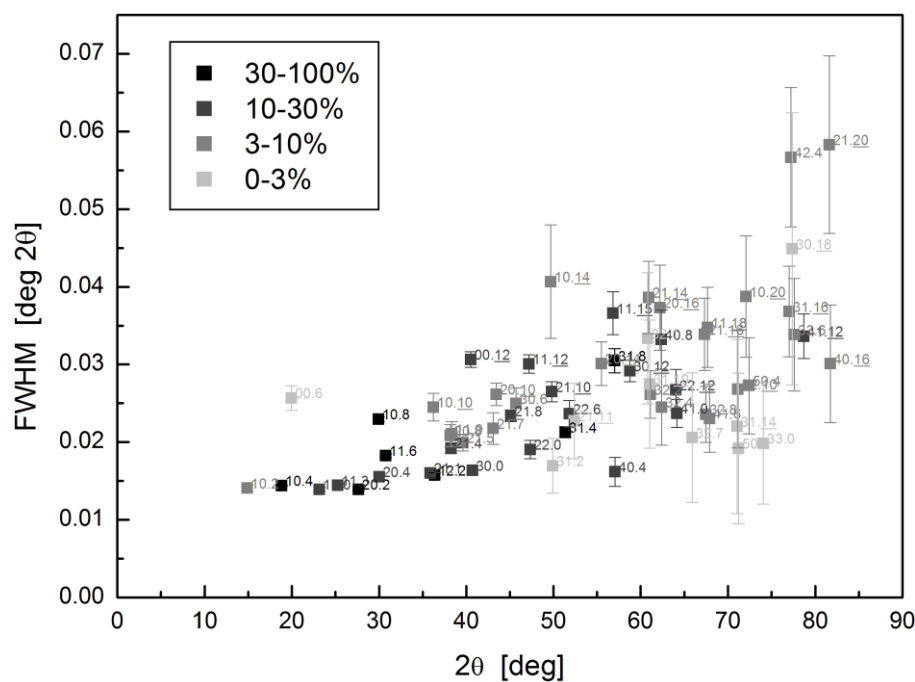

Figure S4. FWHM vs. 2θ plot for CaCO$_3$ during formation. The squares are coloured in grayscale to reflect their relative intensity.
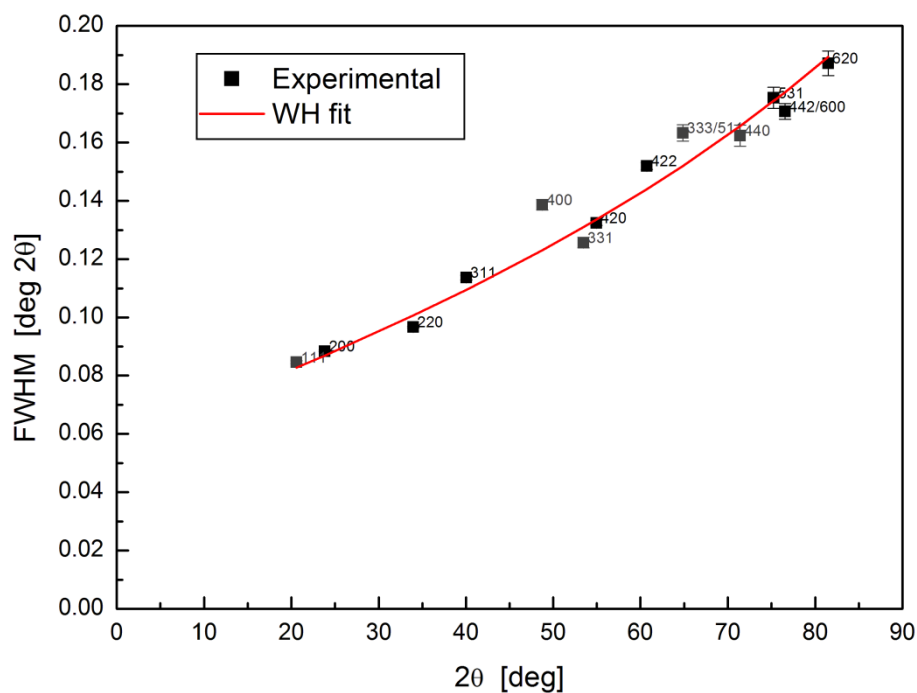
Figure S5. FWHM vs. 2θ plot for CaO during formation. The squares are coloured in grayscale to reflect their relative intensity.

i. Ca(OH)$_2$

The Ca(OH)$_2$ structure consists of hexagonal layers of Ca separated by hydroxyl groups (Figure 1, main text).

hkl-dependent Williamson-Hall plots are not uncommon for layered materials and have been previously observed for Ca(OH)$_2$ [S2]. Stacking faults can frequently occur in the layer stacking direction (c-axis). In addition, the strain may be anisotropic. The data could not be adequately fitted using an isotropic crystallite size and strain model, even when both Gaussian and Lorentzian size and strain components were included.

To account for the possible effects of anisotropic strain, an ellipsoidal model was developed. This was implemented as an envelope function applied to each reflection depending on its angle to the c-axis.
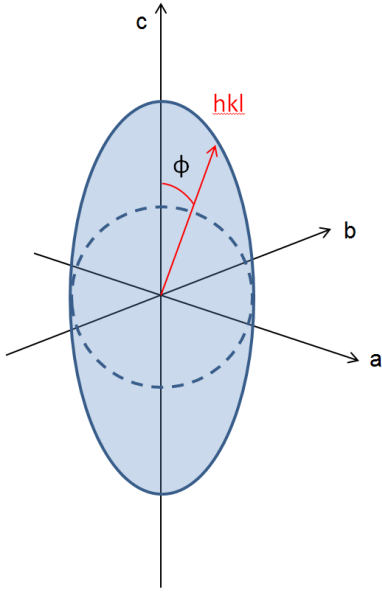
Figure S6. Ellipsoid envelope function, shown relative to the standard isotropic model (dotted line). In this case the aspect ratio (Arat) is approximately 2.

For a hexagonal crystal system, the angle ϕ from any (H,K,L) reflection to the c-axis is given by

$$\cos\phi = \frac{Lc}{\sqrt{(Ha)^2 + 2HKa^2\cos(2\pi/3) + (Ka)^2 + (Lc)^2}}$$

For an ellipsoid with an aspect ratio in the major (c-axis) direction of Arat, the multiplication factor f is

$$f = \frac{1}{\sqrt{\left(\frac{\cos\phi}{Arat}\right)^2 + (\sin\phi)^2}}$$

The ellipsoid model therefore introduces one extra parameter (Arat) for each component where it is used (i.e. Lorentzian/Gaussian, size/strain).

Warren [S3] derived an exact expression for peak broadening due to stacking faults in fcc and hcp metals. (Stacking faults in fcc metals also produce small deviations in the positions of the peaks, but not in hcp metals.) For fcc metals the layers being stacked are the (111) crystal planes, which are hexagonal and can occupy one of three possible positions. For hcp metals the layers being stacked are the (10.0) planes, which are hexagonal and can occupy one of two possible positions. The layered structure of $Ca(OH)_2$ is similar to the latter case, although no exact expression for the peak broadening from the actual value of the stacking fault density can be obtained. We have used Warren's formula directly, noting that although the values obtained for the stacking fault density are likely not in absolute units, the trends observed are useful in interpreting the data.

In the fcc and hcp metals cases, Warren included the stacking fault density as an additive term with the crystallite size broadening.

The final equations for the Lorentzian and Gaussian components of the peak width are therefore:

$$FWHM_{Lor} = \frac{\lambda}{\cos\theta \, CS_{Lor} \, f_{CS\_Lor}} + 4\varepsilon_{Lor}\tan\theta \, f_{str\_Lor} \qquad \text{for H-K = 3n}$$

$$\frac{\lambda}{\cos\theta}\left(\frac{1}{CS_{Lor} \, f_{CS\_Lor}} + \frac{|L|d\,3\alpha_{Lor}}{c^2}\right) + 4\varepsilon_{Lor}\tan\theta \, f_{str\_Lor} \qquad \text{for H-K} \neq \text{3n}$$

$$FWHM_{Gauss}{}^2 = \left(\frac{\lambda}{\cos\theta \, CS_{Gauss} \, f_{CS\_Gauss}}\right)^2 + \left(4\varepsilon_{Gaiss}\tan\theta \, f_{str\_Gauss}\right)^2 \qquad \text{for H-K = 3n}$$

$$\left[\frac{\lambda}{\cos\theta}\left(\frac{1}{CS_{Gauss} \, f_{CS\_Gauss}} + \frac{|L|d\,3\alpha_{Gauss}}{c^2}\right)\right]^2 + \left(4\varepsilon_{Gauss}\tan\theta \, f_{str\_Gauss}\right)^2 \text{ for H-K} \neq \text{3n}$$

where λ is the X-ray wavelength, CS is the crystallite size, $d = \lambda/2\sin\theta$ is the d-spacing, α is the stacking fault density and ε is the strain as a fraction.

The numerical approximation for the width of a Voigt peak based on the Lorentzian and Gaussian component widths is

$$w_{Voigt} \approx 0.5346 w_{Lor} + \sqrt{0.2166 w_{Lor}{}^2 + w_{Gauss}{}^2}$$

From the parameters, the effective crystallite size D_v (i.e. size of the coherent region) and total strain in the minor direction were calculated as follows:

$$\frac{1}{D_v} = \frac{0.5346}{CS_{Lor}} + \sqrt{\frac{0.2166}{CS_{Lor}{}^2} + \frac{1}{CS_{Gauss}{}^2}}$$

$$\varepsilon_0 = 0.5346\varepsilon_{Lor} + \sqrt{0.2166\varepsilon_{Lor}{}^2 + \varepsilon_{Gauss}{}^2}$$

For the major direction, each term (CS_{Lor}, CS_{Gauss}, ε_{Lor}, ε_{Gauss}) is simply multiplied by its appropriate aspect ratio.

The ellipsoidal model with stacking faults was implemented in Topas as follows:

```
macro ApplyHKLFactor(cslor, strlor, aratcl, aratsl, csgauss, strgauss, aratcg,
aratsg, sfdenl, sfdeng){
      ' Major axis of ellipse aligned along c-axis
      ' Angle from (001) to (HKL)
      local phi =
            If(L<0,
      Pi-ArcCos(L*Lpc/Sqrt((Lpa*H)^2+2*Lpa^2*H*K*Cos(2*Pi/3)+(Lpa*K)^2+(Lpc*L)^2)),
```

```
        ArcCos(L*Lpc/Sqrt((Lpa*H)^2+2*Lpa^2*H*K*Cos(2*Pi/3)+(Lpa*K)^2+(Lpc*L)^2)));

        local hklfactorcl = 1/Sqrt((Cos(phi)/aratcl)^2 + (Sin(phi))^2);
        local hklfactorsl = 1/Sqrt((Cos(phi)/aratsl)^2 + (Sin(phi))^2);
        local hklfactorcg = 1/Sqrt((Cos(phi)/aratcg)^2 + (Sin(phi))^2);
        local hklfactorsg = 1/Sqrt((Cos(phi)/aratsg)^2 + (Sin(phi))^2);

        lor_fwhm = If(Mod(H-K,3)==0,
                0.1 Rad Lam/(Cos(Th) cslor hklfactorcl)
                        + Rad 0.04 strlor Tan(Th) hklfactorsl,
                0.1 Rad Lam/(Cos(Th) /(1/(cslor hklfactorcl)
                        + Abs(L)*D_spacing*3*sfdenl/(Lpc^2)))
                        + Rad 0.04 strlor Tan(Th) hklfactorsl
        );
        gauss_fwhm = If(Mod(H-K,3)==0,
                Sqrt((0.1 Rad Lam/(Cos(Th) csgauss hklfactorcg))^2
                        + (Rad 0.04 Tan(Th) strgauss hklfactorsg)^2),
                Sqrt((0.1 Rad Lam/(Cos(Th) /(1/(cslor hklfactorcg)
                        + Abs(L)*D_spacing*3*sfdeng/(Lpc^2))))^2
                        + (Rad 0.04 Tan(Th) strgauss hklfactorsg)^2)
        );
}
```

The prefactors used are as follows: 0.1 to convert Å to nm (wavelength in Å and CS in nm), Rad = $360°/2\pi$ to convert radians to degrees, 0.04 incorporating the strain factor 4 with 0.01 to express strain as a percentage. The Scherrer constant is taken to be 1.

The effect on the FWHM vs. 2θ plots of the ellipsoid model with and without stacking faults is shown in Figures S7-S9.
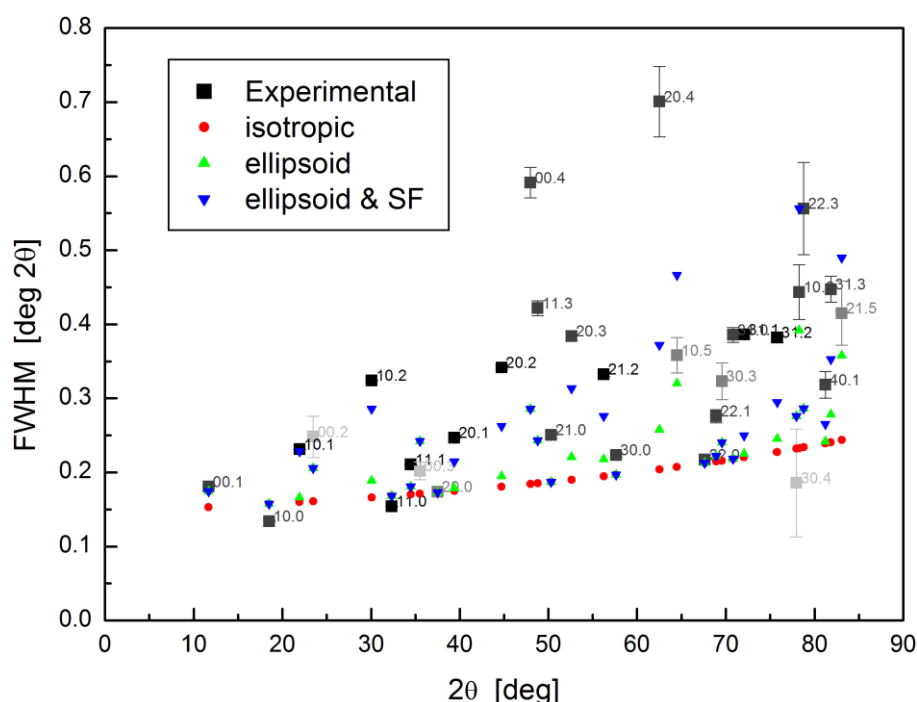

Figure S7. Peak width versus scattering angle for distinct (i.e. non-overlapping) Ca(OH)$_2$ peaks for the starting material. The squares (experimental data points) are coloured in grayscale to reflect their relative intensity. A comparison of the three different models shows the necessity of using both an ellipsoid model and stacking faults.
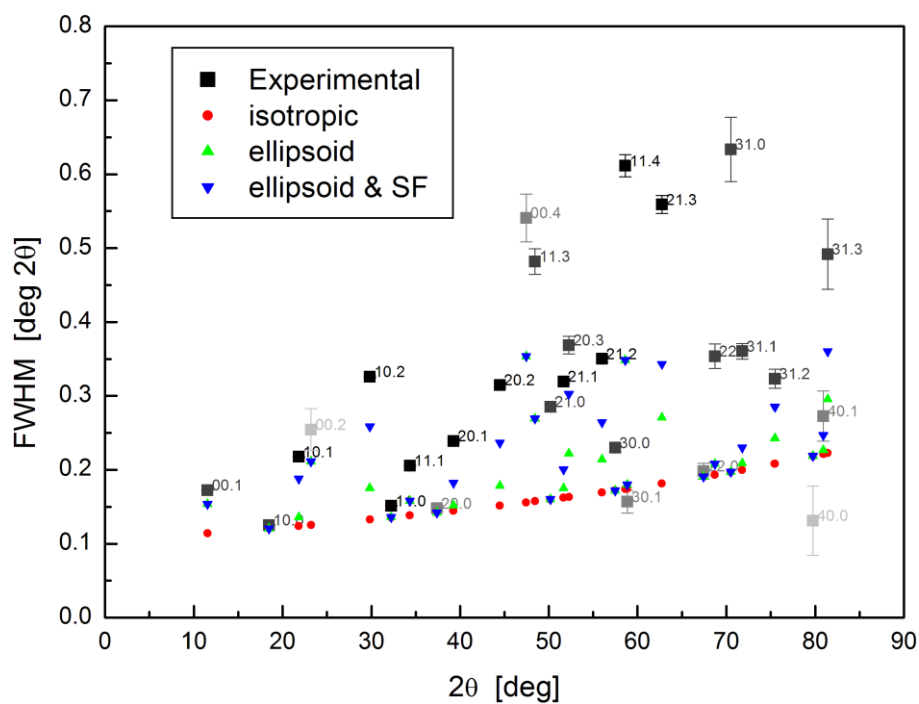
Figure S8. Peak width versus scattering angle for distinct (i.e. non-overlapping) Ca(OH)$_2$ peaks at a temperature corresponding to the onset of carbonation. The squares (experimental data points) are coloured in grayscale to reflect their relative intensity.
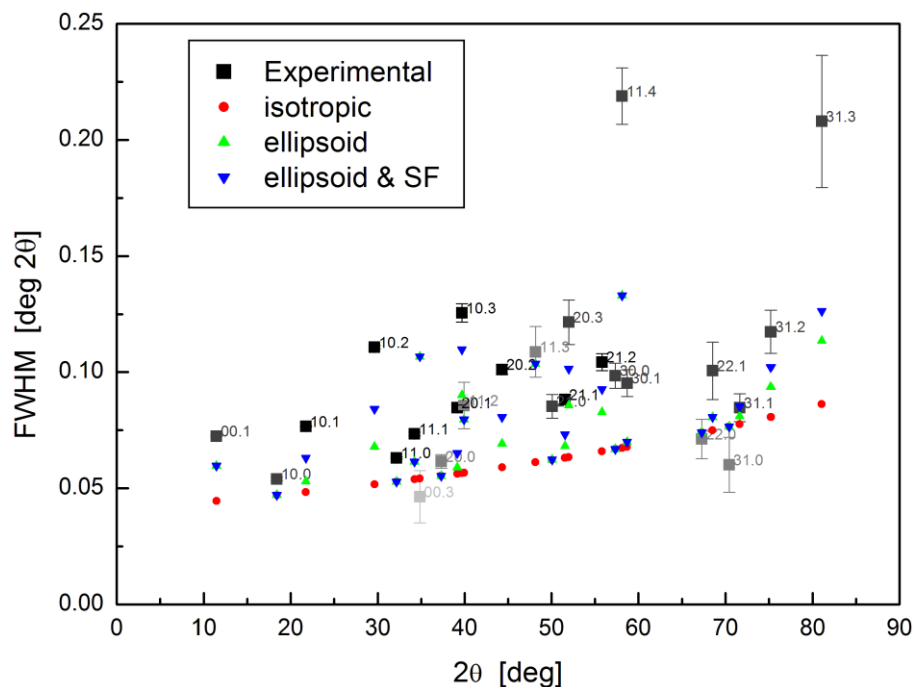

Figure S9. Peak width versus scattering angle for distinct (i.e. non-overlapping) Ca(OH)$_2$ peaks at a higher temperature, when the conversion to CaCO$_3$ is approximately 70% complete. The squares (experimental data points) are coloured in grayscale to reflect their relative intensity.

ii. CaCO$_3$

CaCO$_3$ has a hexagonal crystal structure and exhibits faulting to varying degrees along four different crystal directions (the 10.4, 01.8, 01.2 and 00.1) [S4]. This is often manifested in marked differences in the widths of various peaks. The presence of strain associated with twin faults causes anisotropic peak broadening [S5], but it is difficult to resolve the broadening from the faulting itself from the broadening due to the induced strain [S6]. It is reasonably common in literature for authors to report the peak widths of selected peaks e.g. (10.4) and (00.6), with little further analysis [S7].

We attempted to follow the method of Warren [S3] to derive an expression for the effect on a peak of given (hkl) from faulting on the (10.4) crystal planes, but were unable to. We also attempted the following methods:

1. We used the same ellipsoidal model (without stacking faults) as developed for the Ca(OH)$_2$ phase. The aspect ratio parameters did not vary significantly from 1, indicating that the ellipsoid model was inadequate for describing the peak width anisotropy observed.

2. Scardi et al. [S8] performed whole powder pattern modelling on CaCO$_3$ where the contrast factors $\overline{C}_{hkl}$ were determined from h, k, l and four fitted parameters. The model did not fit our data well, and since these four fitted parameters did not correspond to any physically intuitive values, this method was not pursued further.

3. The method of Dragomir and Ungár [S9] for determining relative dislocation densities from the peak width anisotropy was considered, but since the method relies on prior knowledge of the dislocation contrast factors for each possible slip system in the material, it was not pursued.

4. We noticed that the relative differences between the unaffected peaks (10.2, 10.4, 11.0, 11.3, etc.) and significantly affected peaks (00.6, 10.<u>10</u>, 00.<u>12</u> etc.) were similar when considering a relationship $FWHM \sim \dfrac{1}{D} + c\alpha$ where c is an unknown parameter that is the same for all hkl reflections meeting certain criteria. Interestingly, for the (10.8) reflection a different relation seemed to hold, viz. $FWHM \sim \dfrac{1}{D} + c_2\alpha$ where $c_2 \sim 0.5c$, and for the (11.6) reflection $FWHM \sim \dfrac{1}{D} + c_3\alpha$ where $c_3 \sim 0.25c$. Both the (10.8) and (11.6) reflections are of reasonable intensity. Therefore we attempted to use an empirically derived model using these c factors applied to the stacking fault density (and applied to the 1/cosθ term) for the various reflections meeting the following nested criteria:
   - 10.8   c = 0.5
   - 11.6   c = 0.25
       - Both h and k 0   c = 1
           - L ≤ 6   c = 0
   - Otherwise   c = 0.5 (as an average value)

   This method was abandoned as the values for c for each of these reflections assumed there were no strain effects, which cannot be ruled out.

Our final decision was to ignore the hkl-dependence of the peak width and fit the data using a simple isotropic model. This was made for two reasons: (1) the least-squares fitting method attempts to minimise the sum of the squares of the difference between the fit and the data at each point. For several peaks having reasonable intensity (most notably the (20.2) peak) the experimental intensity was always higher than the model. Deviations were also observed in the residual for the (10.4) peak, due to this very intense peak occurring at low angles where the peak shape is more affected by instrument parameters than peaks at higher angles. The latter effect becomes more pronounced at later times when the peak width decreases. See Figure S10 below. (2) The peaks that show excessive broadening (especially 00.L peaks) are very low intensity. Their contribution to the sum of the squares of the differences is insignificant compared to the differences of intensity of the much stronger peaks due to un-fittable differences in peak height and peak shape described above.
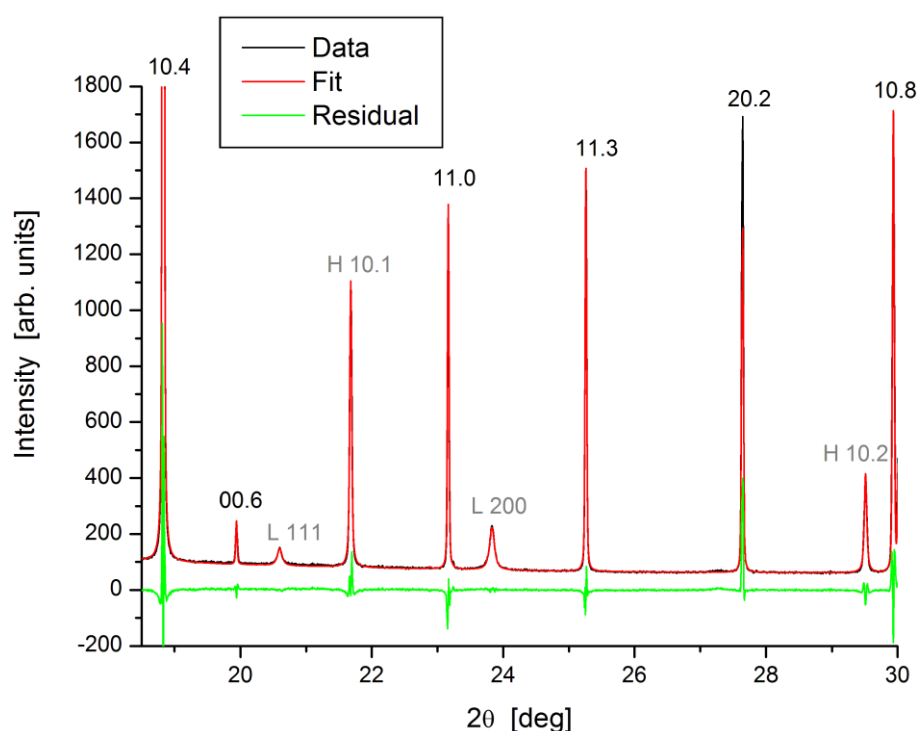

Figure S10. Fit to a scan where CaCO$_3$ is the major component, showing contributions from various peaks to the residual: the slight difference in peak shape for the (10.4) peak (max. intensity 8500 counts) and intensity discrepancy in the (20.2) peaks contribute significantly more than the anisotropic peak width displayed in the FWHM vs. 2θ plots for the (00.6) and (10.8) peaks, among others. Ca(OH)$_2$ ('H') and CaO ('L') peaks are also present.

c. Fitting strategy

i. Global parameters.

The LaB$_6$/diamond wavelength standard was used to fit the beam parameters, including the X-ray wavelength and peak shape parameters. These were implemented in Topas as additional convolutions: a Gaussian with 1/cosθ dependence, a circles convolution with sin(2θ) dependence, and a hat convolution with tanθ dependence. These beam parameters were then fixed for

subsequent fits, together with the Lorentz polarisation factor (90°) and the capillary diameter (0.6 mm).

The linear absorption coefficient was fitted for selected scans (obtained at the start, end, and maximum temperature of each run). It was reasonably consistent across all samples, with an average value of around 70. This value was adopted and fixed for all subsequent fits.

The background used was a 6-parameter Chebychev polynomial, with up to three Lorentzian peaks centred at 2θ values of approximately 14, 29 and 47° to account for the capillary scattering. In addition, the 2θ zero error was fitted.

ii. Model determination for each phase.

Selected scans were fitted, with various parameters allowed to vary. The Topas ellipsoidal macro with stacking faults above offers ten variables, however, not all were required.

Ca(OH)$_2$

There was no statistical difference in the fit when the two Gaussian aspect ratios (for size and strain) were allowed to vary or were fixed to 1 (i.e. isotropic case). When these terms were allowed to vary, the values obtained were extreme, and the uncertainties were often very large (>>100%). Therefore the aspect ratios for both the size and strain ellipsoids were fixed at 1.

In addition, the Gaussian strain itself was very small and with very large reported uncertainties. It was therefore fixed at zero.

In tests where a Gaussian stacking fault term was included as a fitted parameter, it adopted values that were very close to zero, with large reported uncertainties (see Table S1). Therefore the Gaussian stacking fault density was fixed at zero.

Table S1. Goodness-of-fit parameter (r_wp) and stacking fault density values for tests on Ca(OH)$_2$ during a heating run in CO_2. The parameters included in the model were CS$_{Lor}$, CS$_{Gauss}$, str$_{Lor}$, str$_{Gauss}$, AR_CS$_{Lor}$, AR_CS$_{Gauss}$, AR_str$_{Lor}$, AR_str$_{Gauss}$, with sfden_L and/or sfden_G used as indicated.

SF terms:	None	Lorentzian		Gaussian		Both		
Scan/temp	r_wp	r_wp	sfden_L	r_wp	sfden_G	r_wp	sfden_L	sfden_G
0 20°C	4.349	3.810	0.034	4.313	0.045	3.813	0.0345	0.0002
58 270°C	3.955	3.458	0.036	3.956	0.0329	3.458	0.038	0.0001
80 360°C	3.815	3.485	0.027	3.816	0.0117	3.484	0.028	0.0002

Including a Lorentzian stacking fault density made a statistically significant difference to the fit.

Fixing the Lorentzian aspect ratios to 1 (isotropic case) gave little difference for the size, but a significant difference for the strain. Therefore the Lorentzian size aspect ratio was fixed to 1, while the Lorentzian strain aspect ratio was allowed to vary.

Therefore the $Ca(OH)_2$ model used 5 parameters: CS_L, CS_G, Str_L, AR_str_L, and sfden_L.

Figures S11-S14 show some of the parameter values and uncertainties for four test runs on a heating run of $Ca(OH)_2$ in N_2, with the parameters shown in Table S2.

Table S2. Fitted parameters (✓) and fixed values for the four models tested.

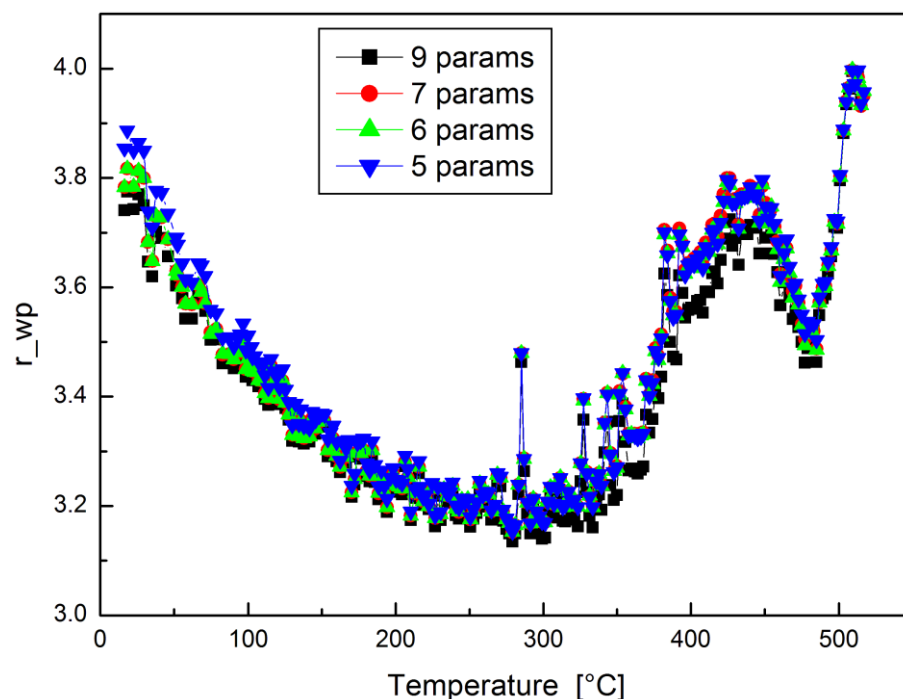|	5-param	6-param	7-param	9-param
Cryst size, Lor	✓	✓	✓	✓
Cryst size, Gauss	✓	✓	✓	✓
Aspect ratio, CS_L	fixed: 1	✓	✓	✓
Aspect ratio, CS_G	fixed: 1	fixed: 1	fixed: 1	✓
Strain, Lor	✓	✓	✓	✓
Strain, Gauss	fixed: 0	fixed: 0	✓	✓
Aspect ratio, str_L	✓	✓	✓	✓
Aspect ratio, str_G	fixed: 1	fixed: 1	fixed: 1	✓
Stacking faults, Lor	✓	✓	✓	✓

Figure S11. Goodness of fit for each of the models, showing insignificant statistical differences between the four.
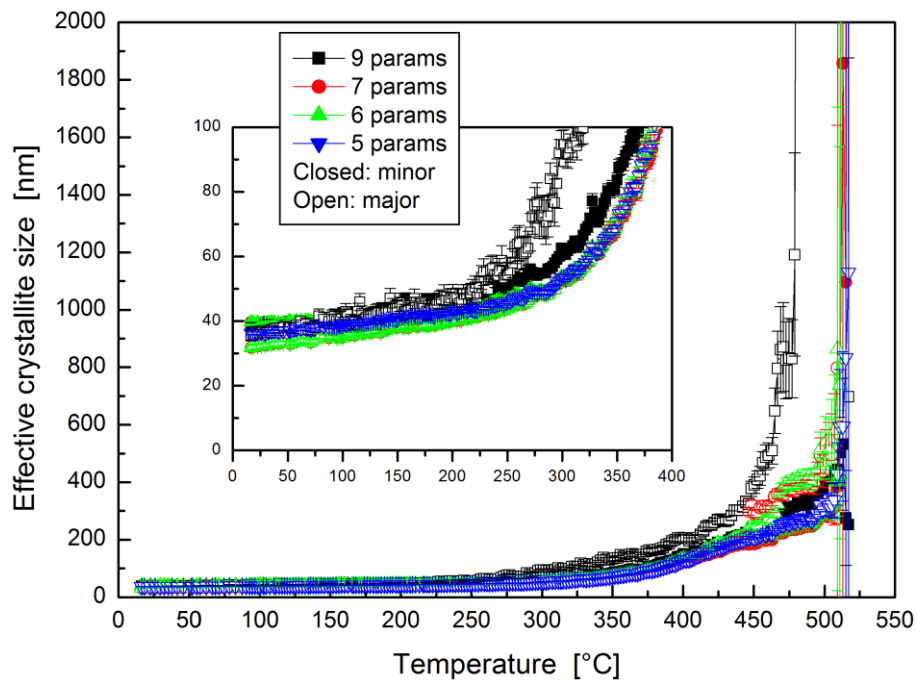
Figure S12. Effective crystallite size (D_v). Note the large variation and large uncertainties for the models with more free parameters.
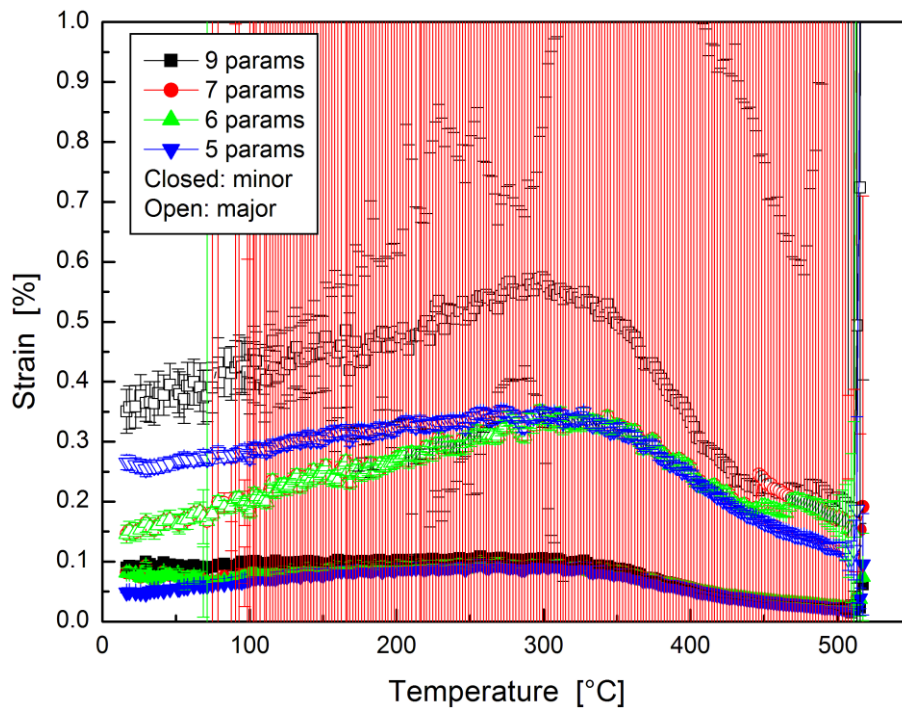

Figure S13. Strain (ε_0). The large uncertainties for the 9- and 7-parameter models are due to the high relative uncertainties associated with the Gaussian strain terms, which have values close to zero.
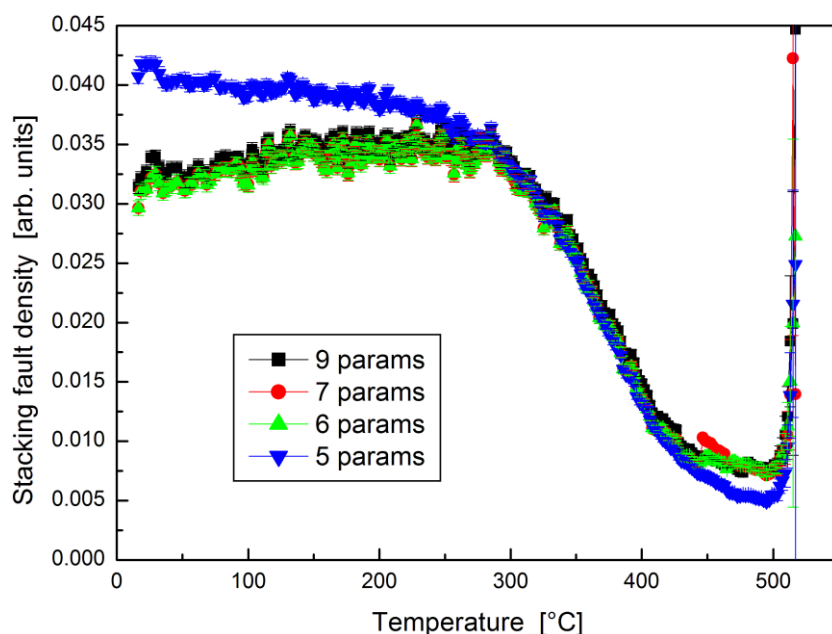
Figure S14. Stacking fault density. The difference between the 5-parameter model and the others at lower temperatures can be explained as follows: In the 5-parameter model, the Lorentzian crystallite size term is isotropic with a higher stacking fault density, whereas in the others it is ellipsoidal, having a smaller crystallite size term in the major direction and lower stacking fault density. The number of faults per crystallite is roughly the same in the two cases.

Other fitted parameters in the for $Ca(OH)_2$ model also included the scale, the lattice parameters, Beq for both Ca and O, the z-co-ordinate for the oxygen atom, and the extent of preferred orientation along the [00.1] direction.

$CaCO_3$

As mentioned above, $CaCO_3$ was fitted using a simpler model, implemented as the Topas macro above with all aspect ratios fixed at unity and all stacking fault densities fixed at zero. Other fitted parameters included the scale, the lattice parameters, Beq for Ca, O and C, the x-co-ordinate for the oxygen atom, and the extent of preferred orientation along the [00.1] direction.

CaO

CaO has the cubic rocksalt structure with both Ca and O atoms occupying special positions. The FWHM vs. 2θ plot (Figure S5) shows no hkl anisotropy. The fitted parameters used were those in the Topas macro above with all aspect ratios fixed at unity and all stacking fault densities fixed at zero, the scale, the lattice parameter, and Beq for Ca and O.

Each individual run was fitted in Topas using a batch file, starting from pre-fitted scans chosen for the phases present in them. These generally proceeded as follows:

	Carbonation run
Start $\rightarrow$ a	Ca(OH)$_2$ only
(a + δ) $\rightarrow$ a, (a + δ) $\rightarrow$ b	Ca(OH)$_2$ + CaCO$_3$
(b + δ) $\rightarrow$ b, (b + δ) $\rightarrow$ c	Ca(OH)$_2$ + CaCO$_3$ + CaO
c $\rightarrow$ end	CaCO$_3$ + CaO

	Dehydration run
Start $\rightarrow$ a	Ca(OH)$_2$ only
(a + δ) $\rightarrow$ a, (a + δ) $\rightarrow$ b	Ca(OH)$_2$ + CaO
b $\rightarrow$ end	CaO only

δ in the tables above represents a small number of scans (approximately 10), since the material that is initially formed may have significant crystallite size or strain effects, meaning that it is best to use an earlier rather than a later scan to fit it during the formation period.

The dehydration run had SiO$_2$ added as a temperature standard (the α-β transition occurs at 573°C, and the α-phase exhibits significant thermal expansion). These phases were fitted in Topas as hkl phases rather than structures, since the large crystallite size present meant that the sample did not present a good powder average and the relative peak intensities changed dramatically during the course of the experiments. An hkl phase allows the lattice parameters to be obtained, which is all that was required from the SiO$_2$ phases.

Therefore the following parameters were fitted in the initial run:

Ca(OH)$_2$ scale, a, c, CS_L, CS_G, str_L, AR_str_L, sfden_L, PO, Ca Beq, O Beq, O_z

CaCO$_3$ scale, a, c, CS_L, CS_G, str_L, str_G, PO, Ca Beq, C Beq, O Beq, O_x

CaO   scale, a, CS_L, CS_G, str_L, str_G, Ca Beq, O Beq

iii. Parameter constraints

After a first pass fitting each scan in a run, the parameters were extracted and assessed.

The March parameter in the preferred orientation for CaCO$_3$ did not deviate significantly from unity in any of the runs. Therefore, the preferred orientation macro was not used for CaCO$_3$. Similarly the x-co-ordinate of the oxygen atom in CaCO$_3$ was stable at a value of 0.2542, so was fixed at this value.

The Gaussian strain for CaO was very small with a large uncertainty. It was therefore fixed at zero.

The Beq (temperature) factors were highly correlated with a number of other parameters, including LAC (when it was fitted in the test runs), crystallite sizes and strains. If allowed to fit for each atom

and each phase, the Beq plots for $CaCO_3$ and CaO had a 'hook' shape (Figure S15). Although it is conceivable that the high values in the initial stages of formation of these phases is real – due to atomic mobility [S10] or static disorder [S11] – the high correlation with other parameters renders this information of limited value, since disorder may also be manifested through the crystallite size and strain terms. Once these phases were established, the Beq trends were similar across the different phases and the different experiments, and the values were similar for $Ca(OH)_2$ and $CaCO_3$. We therefore elected to apply the following constraints:

	$Ca(OH)_2$	$CaCO_3$	CaO
Ca	CaBeq	=CaBeq	=0.5*CaBeq
O	OBeq	=OBeq	=0.4*OBeq
C		=OBeq	

This resulted in a reduction in the number of parameters from seven to two. The relation for CaO was determined empirically, having found to hold for all of the reactions studied.
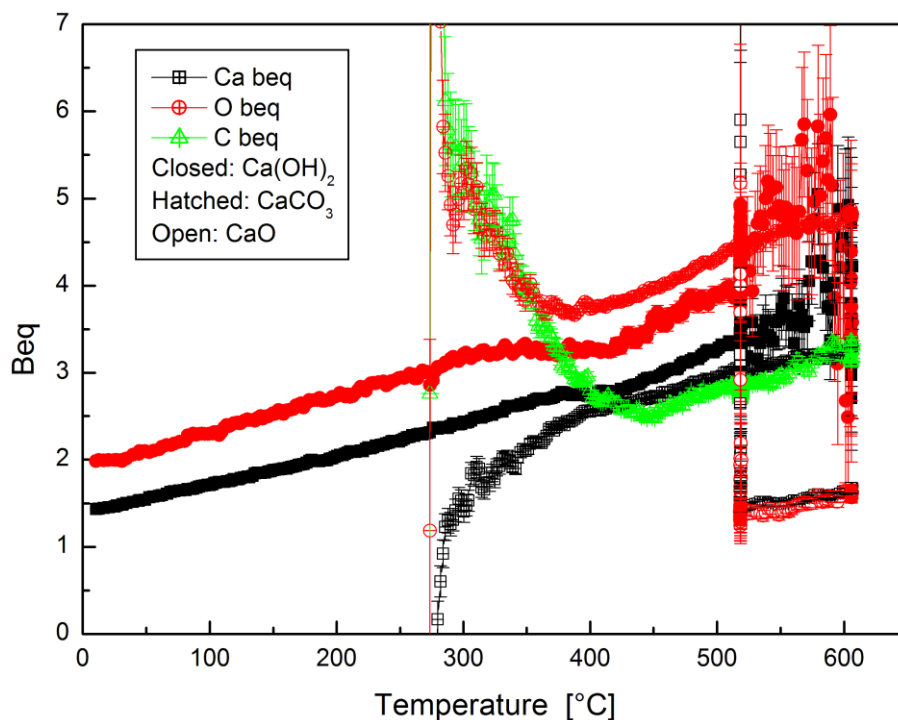
Figure S15. Results for Beq for a carbonation run where the Beq parameter for each atom in each phase was fitted separately.

After re-fitting each scan in the run with these new constraints, those scans where the amount of one phase is small (i.e. formation or consumption regions) were revisited. In these regions it is not appropriate to allow all the parameters to vary and therefore constraints must be applied. The peak positions are defined by the lattice parameters, which are generally the most stable. The least stable parameters are those that contribute the least to peak intensity or peak width, and those that are highly correlated with other parameters. For example, strain is most strongly manifested at high angles of 2θ, but when the peak intensities drop, these high angle peaks are no longer distinguishable.

For Ca(OH)$_2$, the intensities drop significantly as it is consumed. Prior to this the strain and stacking fault density were generally observed to have decreased to low values and plateaued, while the crystallite size had increased to a high value. The preferred orientation and strain aspect ratio also plateaued at constant values. Working forwards in time, first we constrained the preferred orientation and strain aspect ratio; then the strain, stacking fault density and oxygen z-co-ordinate; then the crystallite size parameters; and finally the lattice parameters.

For CaCO$_3$, the intensities increase during its formation. Working backwards in time, first we constrained the strains; then the a lattice parameter (which reached a plateau); then the crystallite size parameters; and finally the c lattice parameter.

For CaO, the intensities increase during its formation. At early times, the crystallite size parameters appear to decrease significantly, which is difficult to explain for the physical system. Working backwards in time, first we constrained the crystallite size parameters; then the strain; and finally the lattice parameter.

4. Examples of fitted data
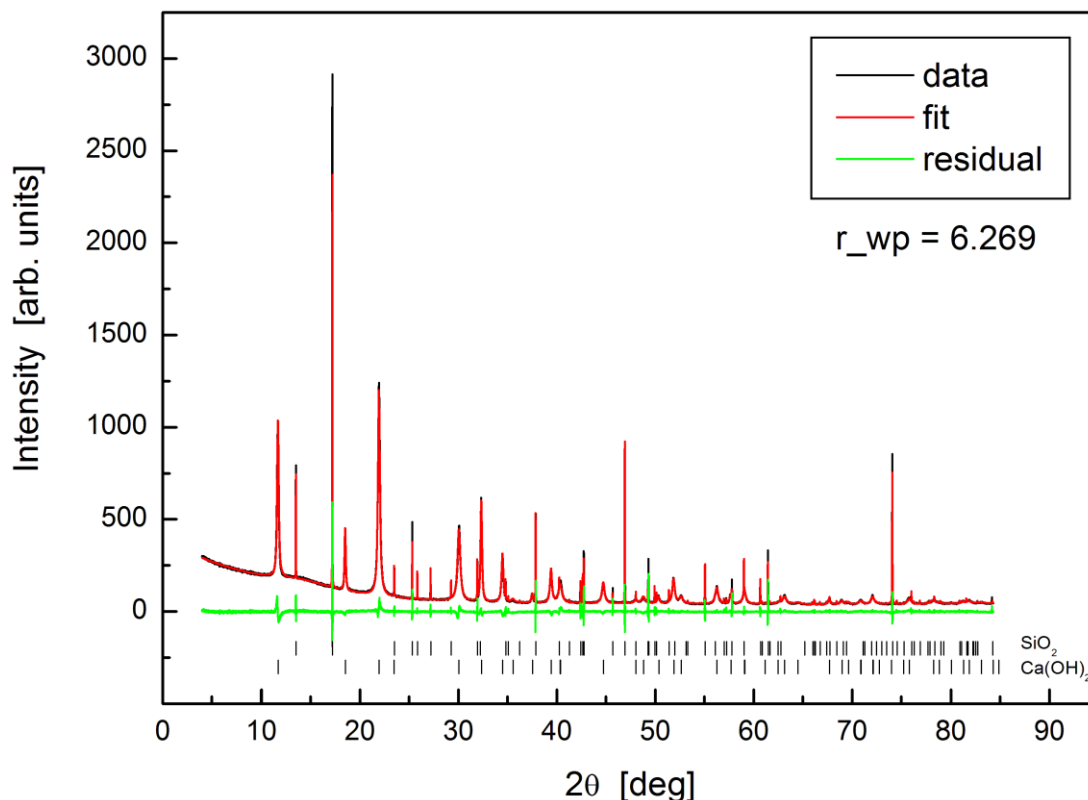
Figure S16. Experimental data, fit, and residual for starting material in dehydration run.
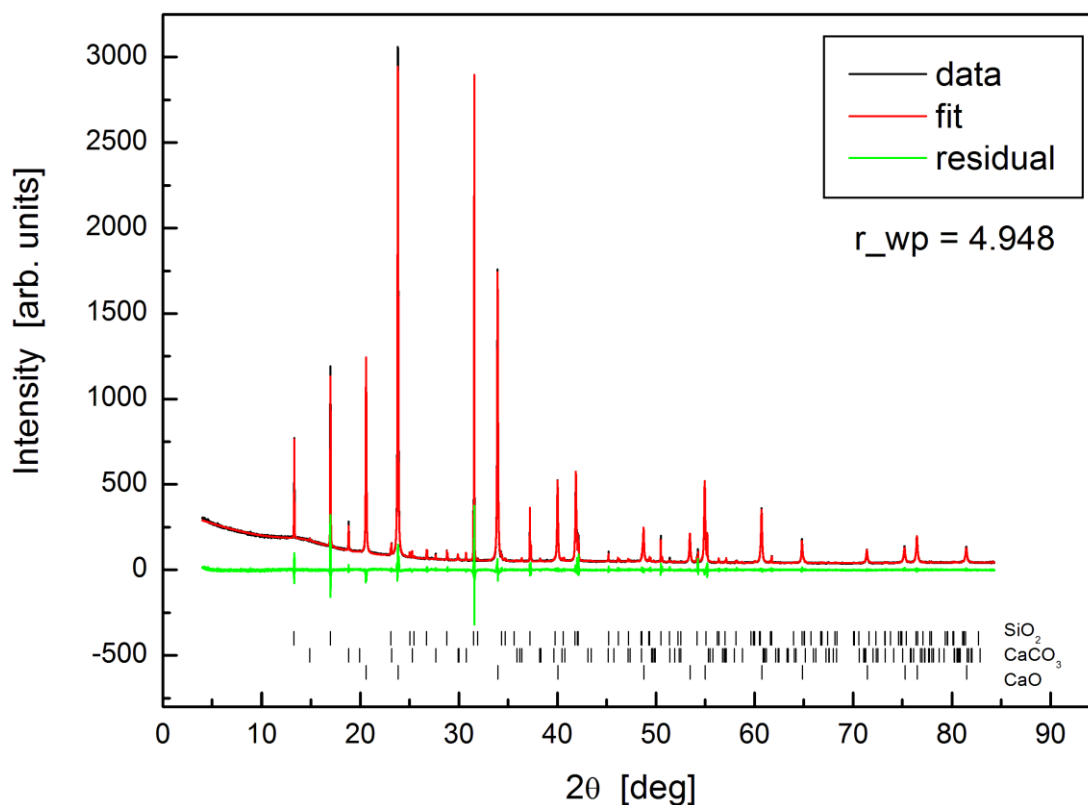
Figure S17. Experimental data, fit, and residual at maximum temperature in dehydration run.
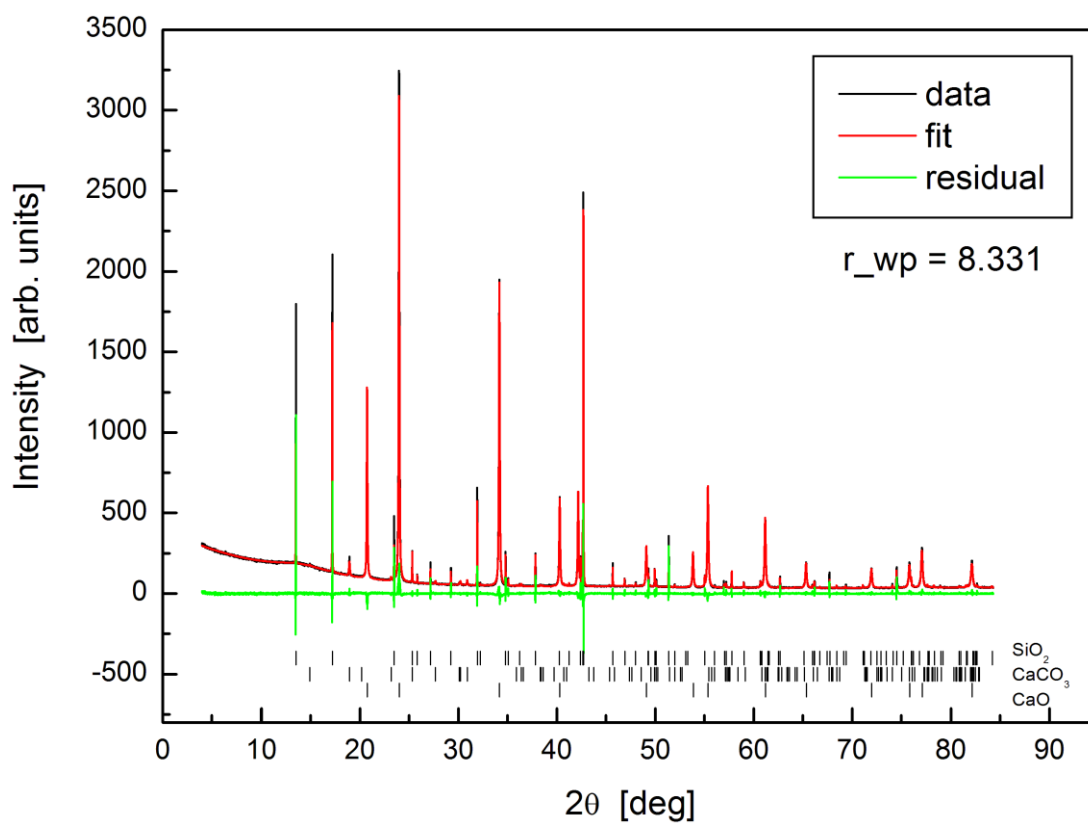

Figure S18. Experimental data, fit, and residual at end of dehydration run after cooling to room temperature.
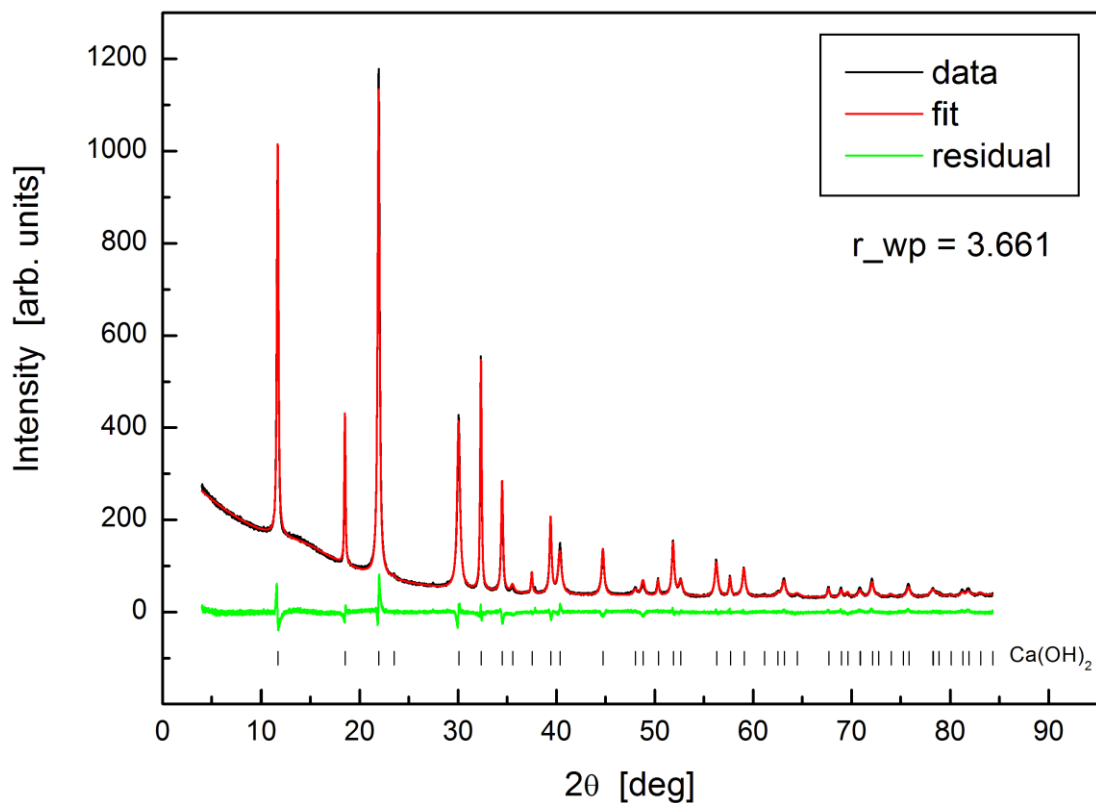
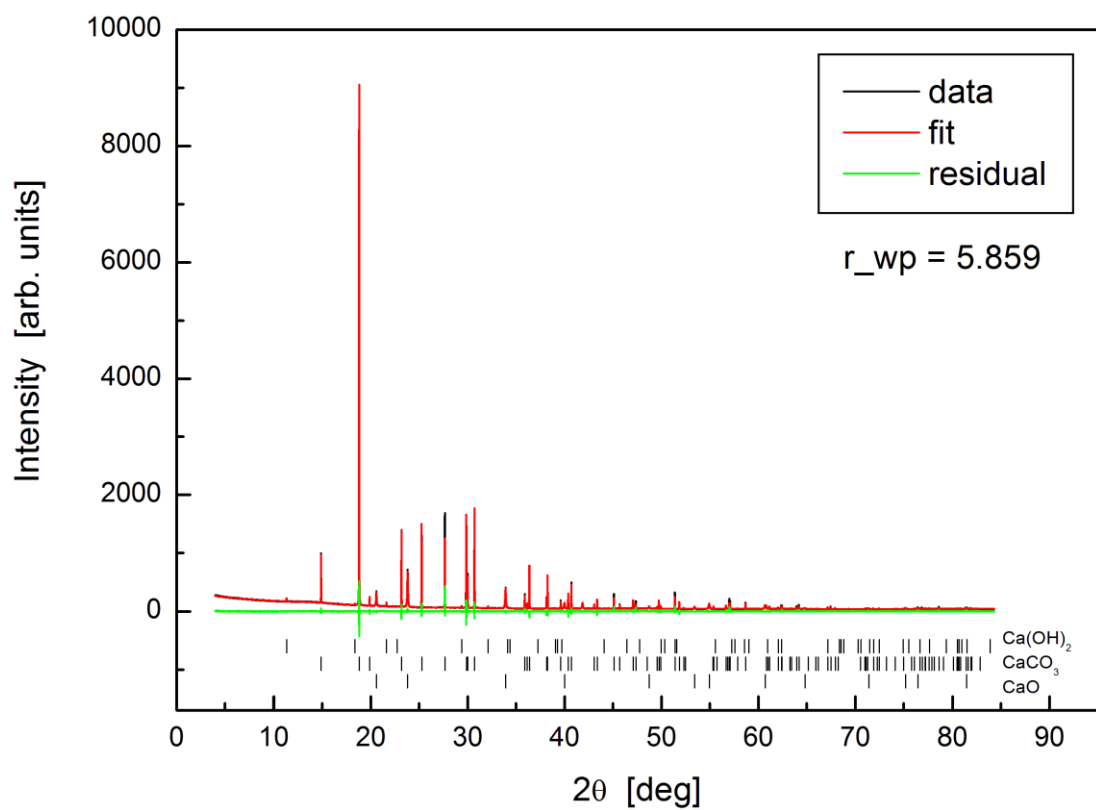Figure S19. Experimental data, fit, and residual for starting material in carbonation run.

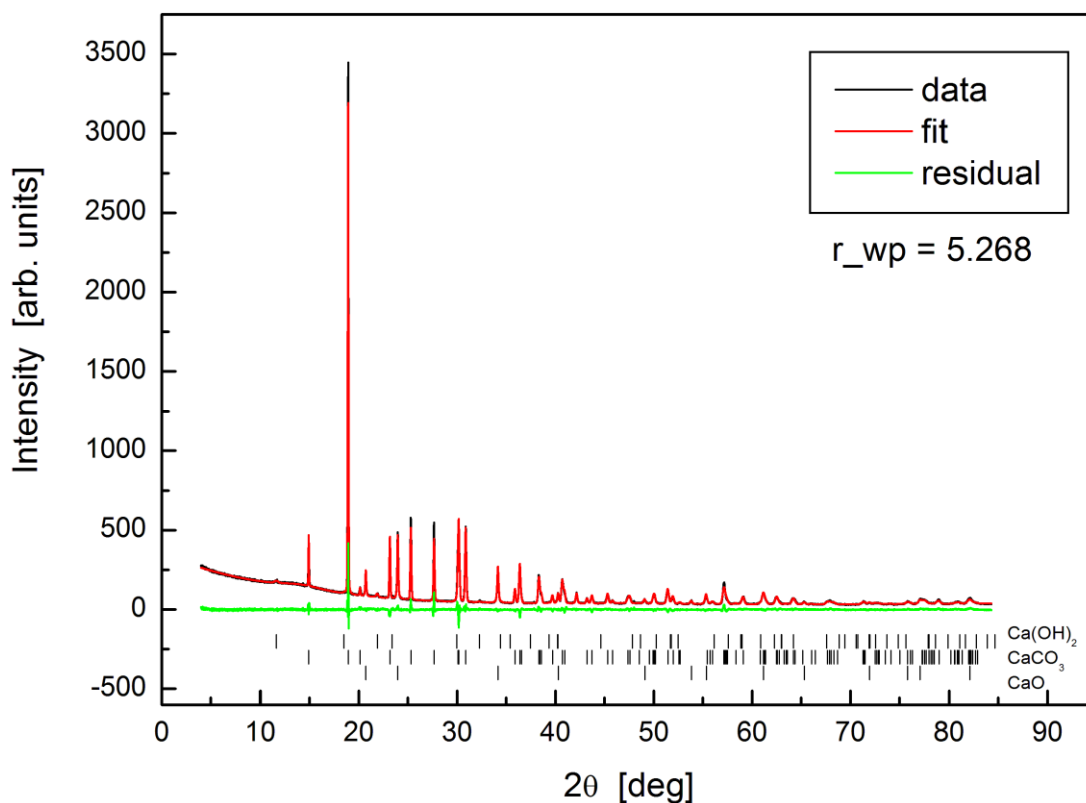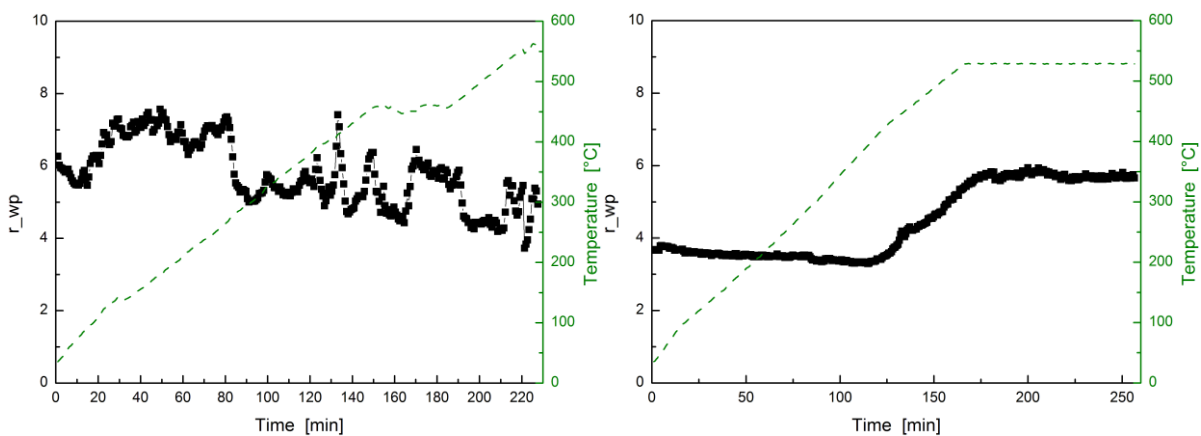Figure S20. Experimental data, fit, and residual at maximum temperature in carbonation run.

Figure S21. Experimental data, fit, and residual at end of carbonation run after cooling to room temperature.

5. Additional parameter results

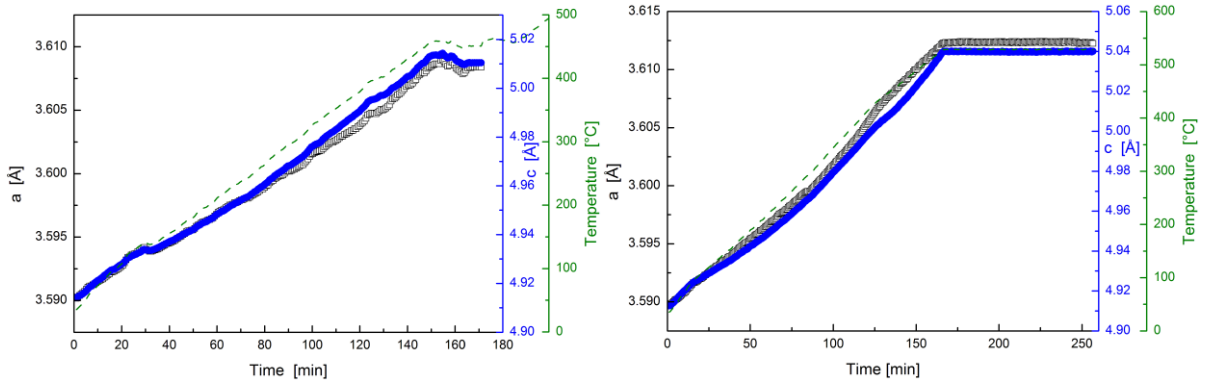Figure S22. Weighted goodness of fit, r_{wp}, for the dehydration run (left) and carbonation run (right).

Figure S23. Ca(OH)$_2$ lattice parameters for the dehydration run (left) and carbonation run (right).
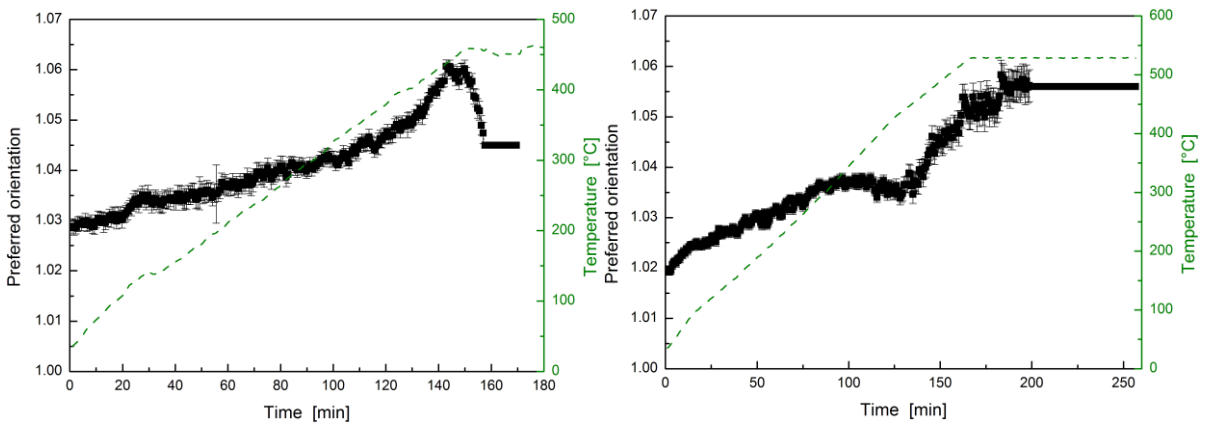

Figure S24. Ca(OH)$_2$ preferred orientation for the dehydration run (left) and carbonation run (right). A value of 1.0 corresponds to no preferred orientation (isotropic system). The parameter was fixed in the later stages where the intensities were small and the uncertainty in this parameter became large.
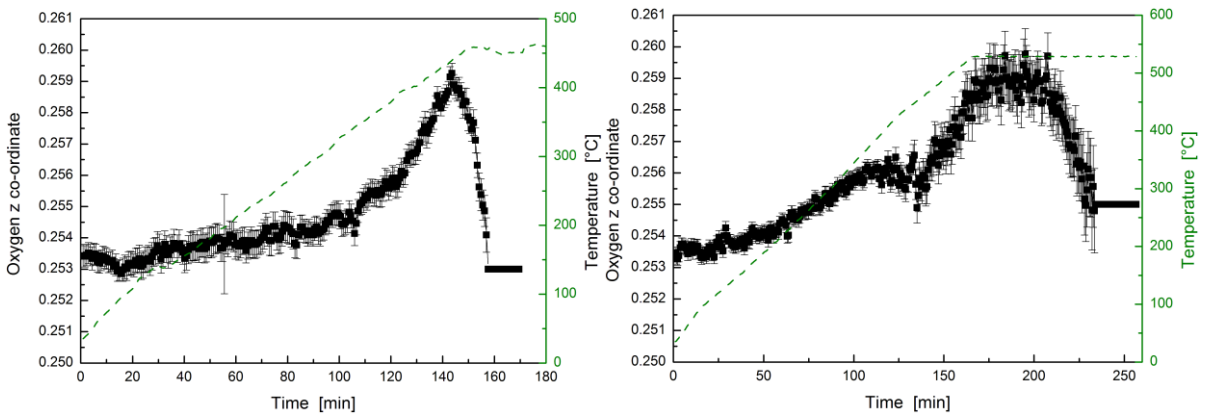

Figure S25. Oxygen z co-ordinate in Ca(OH)$_2$ for the dehydration run (left) and carbonation run (right). The parameter was fixed in the later stages where the intensities were small and the uncertainty in this parameter became large.
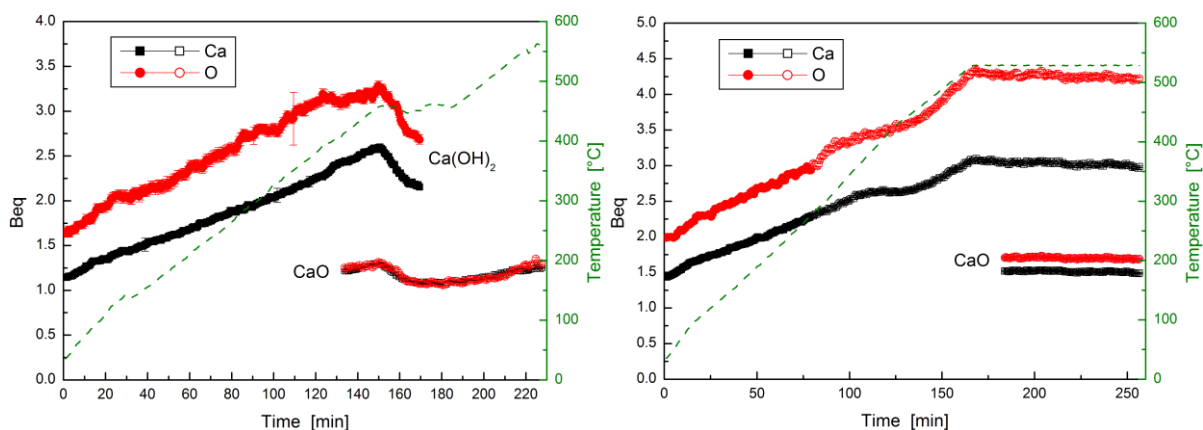
Figure S26. Beq for Ca and O in all phases for the dehydration run (left) and carbonation run (right).

6. Calculated patterns for various defect structures

Patterns were calculated for Ca(OH)$_2$ with various oxygen occupancy levels using PowderCell for Windows 2.3 (Figure S27). The calculated diffraction patterns were normalised to the height of the most intense reflection (the (10.1) peak) and show significant changes in the relative intensities, particularly for the low angle peaks ((00.1) and (10.0), at 11.7 and 18.5 degrees respectively). This is not observed in the experimental data.
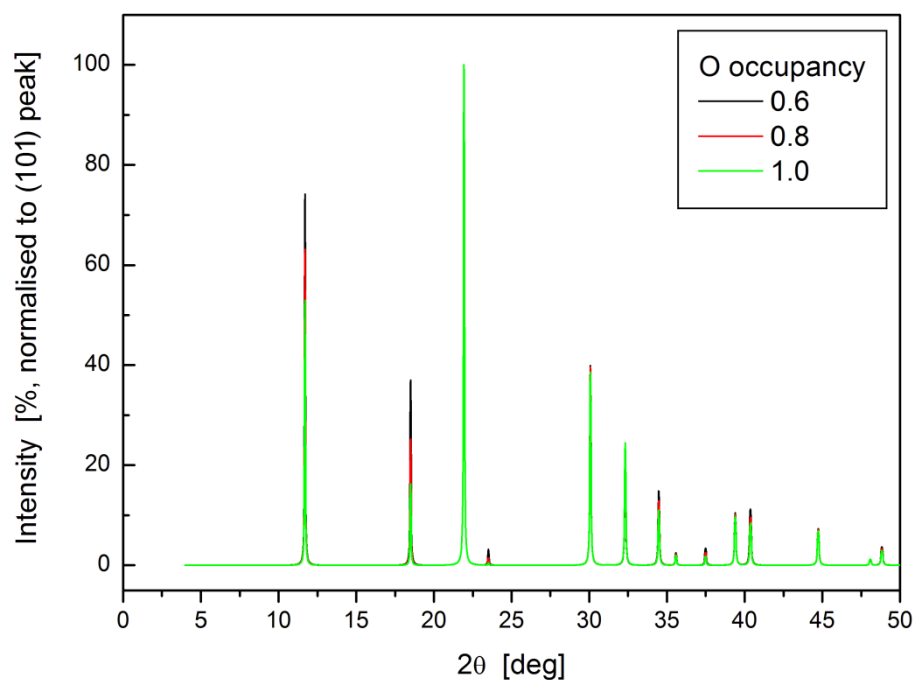

Figure S27. Calculated diffraction patterns for Ca(OH)$_2$ with various oxygen occupancies as indicated.

References

[S1] D. Balzar, N. Audebrand, M. R. Daymond, A. Fitch, A. Hewat, J. I. Langford, A. Le Bail, D. Louër, O. Masson, C. N. McCowan, N. C. Popa, P. W. Stephens and B. H. Toby, J. Appl. Cryst. 37 (2004) 911-924.

[S2] R. Molinder, T. P. Comyn, N. Hondow, J. E. Parker and V. Dupont, Energy Environ. Sci. 5 (2012) 8958-8969.

[S3] B. E. Warren, X-ray Diffraction. Dover Publications Inc., New York (1969), pp. 275-305.

[S4] M. Bruno, F. R. Massaro, M. Rubbo, M. Prencipe and D. Aquilano, Cryst. Growth Design 10 (2010) 3102-3109.

[S5] K. A. Gross, Phil. Mag. 12 (1965) 801-813.

[S6] K. Chen, M. Kunz, N. Tamura and H. R. Wenk, Phys. Chem. Minerals 38 (2011) 491-500.

[S7] Y. Y. Kim, A. S. Schenk, J. Ihli, A. N. Kulak, N. B. J. Hetherington, C. C. Tang, W. W. Schmahl, E. Griesshaber, G. Hyett and F. C. Meldrum, Nature Comm. 5 (2014) 4341.

[S8] H. Pesenti, M. Leoni and P. Scardi, Z. Krist. Suppl. 27 (2008) 143-150.

[S9] I. C. Dragomir and T. Ungár, J. Appl. Cryst. 35 (2002) 556-564.

[S10] F. Goutenoire, O. Isnard, R. Retoux, P. Lacorre, Chem. Mater. 12 (2000) 2575-2580.

[S11] S. Lanfredi, D. H. M. Gênova, I. A. O. Brito, A. R. F. Lima, M. A. L. Nobre, J. Solid State Chem. 184 (2011) 990-1000.